Unraveling the Positive Effects of Glycine Hydrochloride on the Performance of Pb–Sn-Based Perovskite Solar Cells

Kessels, Lana M.; Remmerswaal, Willemijn H.M.; van der Poll, Lara M.; Bellini, Laura; Bannenberg, Lars J.; Wienk, Martijn M.; Savenije, Tom J.; Janssen, René A.J.

Important note
To cite this publication, please use the final published version (if applicable).
Please check the document version above.

Unraveling the Positive Effects of Glycine Hydrochloride on the Performance of Pb–Sn-Based Perovskite Solar Cells

Lana M. Kessels, Willemijn H. M. Remmerswaal, Lara M. van der Poll, Laura Bellini, Lars J. Bannenberg, Martijn M. Wienk, Tom J. Savenije, and René A. J. Janssen*

Additives are commonly used to increase the performance of metal-halide perovskite solar cells, but detailed information on the origin of the beneficial outcome is often lacking. Herein, the effect of glycine hydrochloride is investigated when used as an additive during solution processing of narrow-bandgap mixed Pb–Sn perovskites. By combining the characterization of the photovoltaic performance and stability under illumination, with determining the quasi-Fermi level splitting, time-resolved microwave conductivity (TRMC), and morphological and elemental analysis a comprehensive insight is obtained. Glycine hydrochloride is able to retard the oxidation of Sn^{2+} in the precursor solution, and at low concentrations (1–2 mol%) it improves the grain size distribution and crystallization of the perovskite, causing a smoother and more compact layer, reducing non-radiative recombination, and enhancing the lifetime of photo-generated charges. These improve the photovoltaic performance and have a positive effect on stability. By determining the quasi-Fermi level splitting on perovskite layers without and with charge transport layers it is found that glycine hydrochloride primarily improves the bulk of the perovskite layer and does not contribute significantly to passivation of the interfaces of the perovskite with either the hole or electron transport layer (ETL).

1. Introduction

Mixing lead and tin in metal-halide perovskites results in a narrow-bandgap semiconductor (1.2–1.5 eV). Significant efforts have been dedicated to this class of perovskites to yield high-performing single-junction solar cells and to incorporate them as a sub-cell in all-perovskite multi-junction cells.[1–4] Their fast and easy processing by means of solution processing allows for incorporating various additives to enhance stability and efficiency. However, the addition of tin comes with a set of challenges. First, Sn-containing perovskites tend to crystallize faster than Pb-containing perovskites due to stronger interactions between the SnI_2 and the organic methylammonium iodide (MAI) or formamidinium iodide (FAI) precursors.[5–9] This often results in inhomogeneous films with higher surface roughness. The implementation of dimethyl sulfoxide (DMSO) as a co-solvent with *N,N*-dimethylformamide (DMF) allows the retardation of the crystallization by intervening with the MAI/FAI-SnI_2 complex.[5,10] Second, Sn^{2+} has a lower oxidation potential than Pb^{2+}. With the slightest amounts of oxygen, Sn^{2+} oxidizes to Sn^{4+}, thereby causing Sn vacancies.[11] At the perovskite surface, Sn vacancies cause non-radiative recombination, while in the bulk Sn^{4+} can cause p-doping ($Sn^{4+} \rightarrow Sn^{2+} + 2h^+$), and Sn vacancies can cause degradation of the crystal lattice.

To avoid these detrimental effects, extensive research focusses on the use of bulk passivators to prevent the oxidation of Sn^{2+}, or to reduce Sn^{4+} back to the favorable Sn^{2+} oxidation state. Besides the commonly employed reducing agents such as tin fluoride (SnF_2) or metallic tin, the use of zwitterionic molecules has proven to be successful. One of the first published zwitterionic molecules used in Pb–Sn perovskites was formamidine sulfinic acid reported by Xiao et al.[2] The distinct functional groups allow for multiple interactions with the perovskite precursors or with the transport layers, resulting in more crystalline domains and better charge transport.

L. M. Kessels, W. H. M. Remmerswaal, L. Bellini, M. M. Wienk,
R. A. J. Janssen
Molecular Materials and Nanosystems and Institute for Complex
Molecular Systems
Eindhoven University of Technology
P.O. Box 513, 5600 MB Eindhoven, The Netherlands
E-mail: r.a.j.janssen@tue.nl

The ORCID identification number(s) for the author(s) of this article can be found under https://doi.org/10.1002/solr.202400506.

L. M. van der Poll, T. J. Savenije
Department of Chemical Engineering
Faculty of Applied Sciences
Delft University of Technology
Van der Maasweg 9, 2629 HZ Delft, The Netherlands

L. J. Bannenberg
Department of Radiation Science and Technology
Faculty of Applied Sciences
Delft University of Technology
Mekelweg 15, 2629 JB Delft, The Netherlands

R. A. J. Janssen
Dutch Institute for Fundamental Energy Research
De Zaale 20, 5612 AJ Eindhoven, The Netherlands

Since then, amino acids, another class of zwitterionic molecules, have gained popularity in preparing narrow-bandgap perovskites, but also other reducing agents such as 2,5-di-tert-butylhydroquinone have been used successfully for this purpose.[12] Amino acids have already shown to work well for the traditional MAPbI$_3$ perovskites. For instance, Lin et al. showed that when 5-aminovaleric acid was added to the bulk, it passivates grain boundaries to limit oxidative degradation and thus extend the lifetime.[13] However, the long aliphatic chain reduced the short-circuit current density (J_{SC}). In a follow-up study by Lin et al. the carbon chain length was reduced from four (5-aminovaleric acid) to three (γ-aminobutyric acid), two (β-alanine), and one (glycine) carbon atoms. All amino acids gave similar protection against oxygen-induced degradation, but the amino acids with shorter aliphatic chains yielded larger grains and thereby enhanced J_{SC}.[14] Comparing glycine with proline, Yuan et al. discovered that steric hindrance of cyclic proline enhanced its complexation with lead, resulting in even larger grain sizes and more preferred crystal orientation compared to linear glycine.[15] In recent years, glycine has also been added to Pb–Sn mixtures in binary additive systems.[16–18] Kim et al. combined glycine hydrochloride (GlyHCl) with copper thiocyanate (CuSCN) in a hole transport layer (HTL) free Pb–Sn perovskite solar cell to promote hole extraction and suppress non-radiative recombination.[16] Furthermore, Hu et al. combined GlyHCl with ethylene diammonium diiodide (EDAI$_2$) as the top passivator to improve both the bottom and top interface of the perovskite layer.[17] They reported that addition of GlyHCl to the perovskite bulk not only creates nucleation centers, as seen with lower-dimensional perovskites,[19] but also that GlyHCl interacts with the poly(3,4-ethylenedioxythiophene):poly(styrene sulfonate) (PEDOT:PSS) HTL to facilitate hole extraction. However, at present, the effects of GlyHCl on the properties of the Pb–Sn perovskite bulk and its interfaces with the HTL and, especially, the electron transport layer (ETL) are not fully explored. Understanding the function of additives like GlyHCl can help the development of even more promising additives.

Herein, the influence of GlyHCl and its concentration in the precursor solution on the device performance and stability and on the crystallinity, micro-strain, charge carrier mobility, and non-radiative recombination losses of Pb–Sn perovskite layers are investigated. It is found that small amounts of the GlyHCl enhance the open-circuit voltage (V_{OC}) to 0.81 V and fill factor (FF) to 0.78, obtaining a power conversion efficiency (PCE) of 17.4% that remains stable for at least 10 min. X-ray photoelectron spectroscopy (XPS), (light intensity-dependent) absolute photoluminescence (PL), and time-resolved microwave conductivity (TRMC) were used to determine the origin of the performance and stability. It is observed that 1–2 mol% of GlyHCl improves the crystallization of the perovskite to obtain a smoother and more compact film and also reduces non-radiative recombination in the bulk. However, larger amounts of GlyHCl cause an excess of the material on the top surface, thereby introducing recombination centers and limiting charge extraction, leading to low V_{OC}.

2. Results and Discussion

A Cs$_{0.1}$FA$_{0.6}$MA$_{0.3}$Pb$_{0.5}$Sn$_{0.5}$I$_3$ (MA being methylammonium and FA formamidinium) narrow-bandgap perovskite was fabricated following the reported composition and recipe of Hu et al.[17] Ammonium thiocyanate (NH$_4$SCN) at 2 mol% relative to the total metal (PbI$_2$ and SnI$_2$) concentration was used to control the nucleation and growth of the perovskite grains.[20,21] SnF$_2$ was added to improve the crystallinity and because of its ability to reduce Sn^{4+} to Sn^{2+} in the precursor solution to lower the amount of Sn vacancies in the resulting perovskite film.[22–25] However, the often-used concentration of 10 mol% SnF$_2$ relative to the SnI$_2$ concentration was lowered to 5 mol% because this yielded higher performing and more stable devices. Perovskite films were made using a one-step anti-solvent method as detailed in the Experimental Section. To investigate the influence of GlyHCl on the perovskite formation and crystallization process, the salt was directly added to the precursor solution. This was done to enable the integration of the salt into the perovskite complexation process, either in powder form or when dissolved in a DMF/DMSO mixture.

First, the influence of GlyHCl on the photovoltaic performance was studied by adding 0, 0.5, 1, 2, or 4 mol% GlyHCl to the precursor solution relative to the total metal (PbI$_2$ and SnI$_2$) concentration. Solar cells with a p-i-n configuration were fabricated on glass substrates with an indium tin oxide (ITO) front electrode, covered with PEDOT:PSS as HTL. For electron extraction, a bi-layer consisting of C$_{60}$ and bathocuproine (BCP) was used in combination with an Ag back electrode (**Figure 1**a). The current density−voltage (J–V) characteristics and external quantum efficiency (EQE), show that the best performance in terms of PCE was achieved using 2 mol% GlyHCl providing a PCE of 16.0%. This represents an improvement compared to the 13.9% for the reference cell without GlyHCl (Figure S1 and Table S1, Supporting Information). By using 2 mol% GlyHCl, the V_{OC} increased from 0.69 to 0.76 V and the FF from 71% to 75%, but the J_{SC} slightly decreased. An initial stability test was performed by illuminating the devices while keeping them at the initial maximum-power-point voltage (V_{MPP}) for 10 min (Figure S1c, Supporting Information). Interestingly, the current density decreased with time when less than 2 mol% GlyHCl was used, but upon the addition of 2 or 4 mol% it stabilized with no loss in the first 10 min. Additionally, V_{OC} tracking was performed (Figure S1d, Supporting Information). The values at $t = 0$ matched the V_{OC} obtained from the J–V measurements, but the V_{OC} rapidly decreased for the devices processed with 0, 0.5, and 1 mol% GlyHCl. Again, the devices with 2 and 4 mol% maintained a stable V_{OC}.

While optimizing the processing conditions, we found that replacing NH$_4$SCN with guanidinium thiocyanate (GuaSCN) enhanced the stability while preserving the performance.[26,27] Experimenting with the annealing temperatures showed that higher PCEs could be obtained when the dual annealing technique was reversed to first anneal 10 min at 65 °C and then 10 min at 100 °C. This gradual heating of the film allowed for a more controlled crystallization resulting in a more homogenous, compact, and smoother film. A similar effect was observed when the application of the anti-solvent was delayed from the original 43 to 51 s. When the two were combined, an increase in performance was achieved. We then tested the effect of different concentrations of the various additives (SnF$_2$, NH$_4$SCN, and GuaSCN) on the PCE using the optimized processing conditions. Without SnF$_2$, the PCE did not exceed 3%. We found that 5 mol%
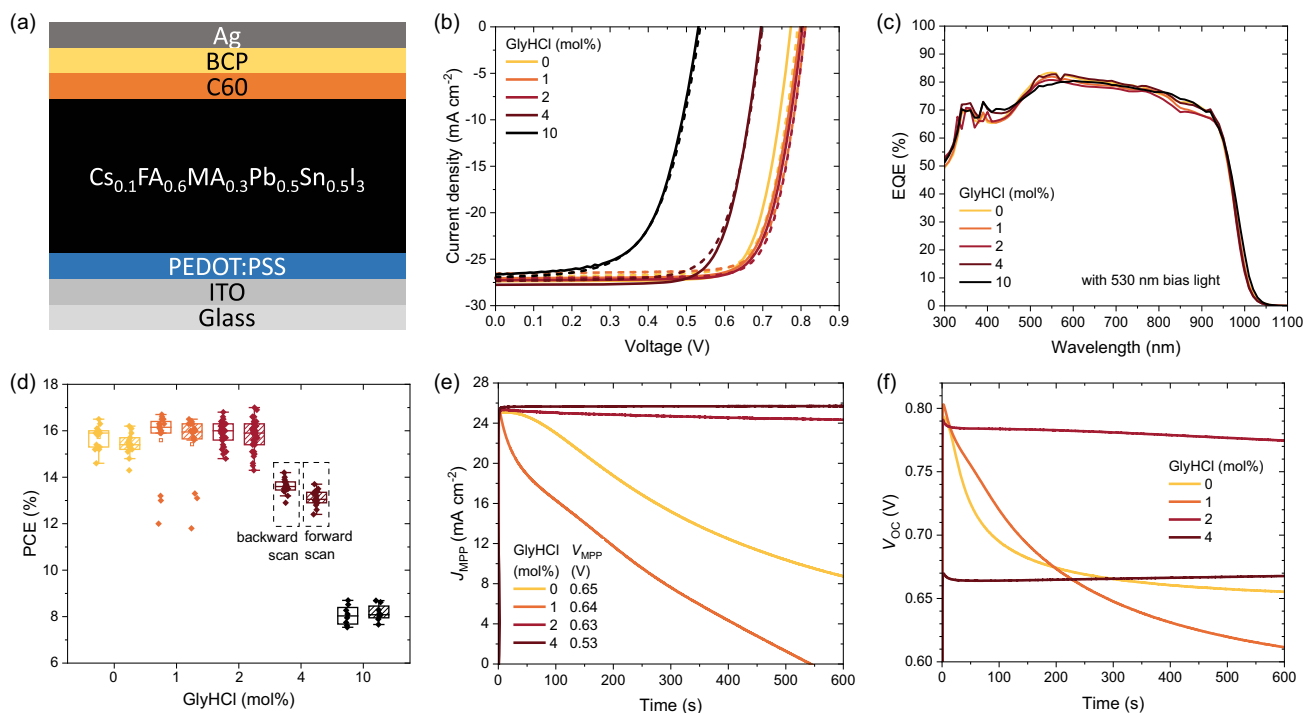
Figure 1. a) Schematic of the p-i-n device stack. b) Current density–voltage characteristics recorded in forward (dashed lines) and backward (solid lines) scan directions of the best performing $Cs_{0.1}FA_{0.6}MA_{0.3}Pb_{0.5}Sn_{0.5}I_3$ solar cells, processed with 2 mol% GuaSCN, 5 mol% SnF_2, and 0, 1, 2, 4, or 10 mol% GlyHCl. c) External quantum efficiency of the same devices under 530 nm light bias. d) Statistics on the PCE of all devices fabricated. e) Current density tracking of the devices with the voltage set at the initial maximum-power-point voltages (V_{MPP}) as shown in the legend, measured one day after fabrication. f) Open-circuit voltage tracking of the same devices, measured on the second day after fabrication.

SnF_2 was the optimum concentration (Figure S2 and Table S2, Supporting Information). Devices fabricated with varying concentrations of NH_4SCN or GuaSCN, in addition to 5 mol% SnF_2, show a less strong effect on the PCE. Marginal differences in PCE were found between 1 mol% NH_4SCN and 2 mol% GuaSCN, but replacing NH_4SCN by GuaSCN enhanced the stability (Figure S3 and Table S3, Supporting Information) in accordance with previous results.[25,26]

Using this adapted procedure, devices processed with 0, 1, 2, 4, and 10 mol% GlyHCl were fabricated, resulting in an increase

in V_{OC} and FF and small variations in J_{SC} and EQE (Figure 1b,c and **Table 1**). Increasing the GlyHCl concentration results in a small increase of layer thickness but the roughness of about 20 nm is constant (Table S4, Supporting Information). Based on the second derivative of the EQE spectrum the bandgap is 1.27 eV. The PCE statistics are shown in Figure 1d for the forward and backward scan directions and the detailed device statistics are collected in Table S5 (Supporting Information). Using GuaSCN, the V_{OC} of the reference increased further to 0.79 V, yielding a PCE of 16.9% and an average performance of

Table 1. Photovoltaic parameters of champion devices with a narrow bandgap perovskite processed with 2 mol% GuaSCN, 5 mol% SnF_2, and 0, 1, 2, 4, or 10 mol% GlyHCl.

GlyHCl [mol%]	Scan	J_{SC} [mA cm^{-2}]	V_{OC} [V]	FF [−]	PCE [%]	$J_{SC, EQE}$ [mA cm^{-2}]	PCE$_{EQE}$ [%]
0	Backward	27.4	0.77	0.77	16.3	28.21	16.7
	Forward	26.9	0.79	0.76	16.2		16.9
1	Backward	27.0	0.80	0.76	16.5	27.85	16.9
	Forward	26.6	0.81	0.77	16.5		17.4
2	Backward	27.3	0.80	0.77	16.8	27.51	16.9
	Forward	27.1	0.81	0.78	17.0		17.4
4	Backward	27.8	0.70	0.73	14.2	28.35	14.5
	Forward	27.3	0.70	0.72	13.7		14.1
10	Backward	26.6	0.53	0.62	8.7	28.21	9.3
	Forward	26.9	0.54	0.60	8.7		9.1

$15.7 \pm 0.5\%$. Also, when using GuaSCN, 2 mol% GlyHCl remained the optimum additive concentration, providing a V_{OC} of 0.81 V and an FF of 0.78 for the champion device with a PCE of 17.4% and an average PCE of $15.9 \pm 0.5\%$. We note that these PCEs have been obtained without any specific top-passivation with agents such as EDAI$_2$[17] or CdI$_2$,[28] which are known to increase V_{OC} by passivating the interface between the Pb–Sn perovskite and the C$_{60}$ ETL. When more than 2 mol% of GlyHCl was added, the V_{OC} dropped. The EQE-integrated J_{SC} varied slightly with amounts of GlyHCl added, but without a clear trend. The shape of the EQE spectra remained the same for the different concentrations (Figure 1c) and the EQE was virtually independent of the light bias used. When an anti-reflection coating (ARC) was applied to the front side of the solar cells, the EQE increased over the whole spectrum, gaining 1 mA cm^{-2} in J_{SC}, resulting in a maximum PCE of 18.7% (Table S6 and Figure S4, Supporting Information).

Tracking the V_{OC} and the photocurrent (J_{MPP}) at the initial V_{MPP} of devices processed with GuaSCN for 10 min (Figure 1e,f) resulted in the same trend as observed for NH$_4$SCN. With 0 or 1 mol% GlyHCl both J_{MPP} and V_{OC} rapidly decrease, but the stability is considerably enhanced when 2 or 4 mol% GlyHCl are used, with a maximum loss of 5%. By performing multiple J–V measurements before and after J_{MPP} and V_{OC} tracking, we found that the device processed with 2 mol% GlyHCl showed an almost negligible permanent decrease and recovered from the loss during the tracking (Figure S5, Supporting Information). The higher stability of the cells with 2 and 4 mol% GlyHCl seen in Figure 1e,f are attributed to an improved layer quality. The J–V sweeps performed before and after J_{MPP} and V_{OC} tracking (Figure S5, Supporting Information) show that the changes seen for 0 and 1 mol% GlyHCl in Figure 1e,f are partly reversible. Such reversible changes and the timescale at which they occur initially (<10 min) are typical for the presence of mobile ions and/or mobile charged vacancies.

Clearly, the use of GlyHCl and its concentration affect the performance and device stability. One explanation can be that the acid group of the glycine binds strongly with the Sn^{2+} and thereby suppresses oxidation just like other zwitterionic molecules have shown.[2,19] To investigate the effect of GlyHCl on the oxidative stability of Sn^{2+}, SnI$_2$ beads with or without GlyHCl were dissolved in DMF (vials 1–3) or DMSO (vials 4–6) under nitrogen conditions, resulting in yellow or colorless solutions, respectively (Figure S6, Supporting Information). For a direct comparison, solutions of SnI$_2$ with SnF$_2$ in DMF and DMSO were also made, because SnF$_2$ is known for its strong reducing character.[22–25] The solutions were then exposed to oxygen for about 30 s and shaken to speed up the diffusion of the oxygen into the solution (Figure S6, Supporting Information). Within minutes, the vial with only SnI$_2$ in DMF turned orange and at 3 min the solution was colored dark orange, a clear sign of the oxidation of Sn^{2+} to Sn^{4+}.[29–33] Simultaneously, the 0.18 M GlyHCl solution with SnI$_2$ showed minimal discoloration within the first 3 min, and only at 4 min a light orange color was observed. While both solutions turned darker with time, the one with SnF$_2$ remained yellow. Additionally, a white precipitate, most likely Sn(IV)F$_4$ formed, which turned orange over time. For the solutions in DMSO, the first color change was observed after

8 min for the SnI$_2$ solution which obtained a slightly yellow color. The increased stability against oxidation is attributed to the stronger interaction between DMSO and SnI$_2$ compared to DMF and SnI$_2$. We note that DMSO itself has been found to be somewhat oxidizing at higher temperatures under acidic conditions,[30,34] but at room temperature DMSO apparently retards oxidation of SnI$_2$ by air. For the GlyHCl-containing DMSO solution of SnI$_2$ the slight yellow color was only seen after 2 h, indicating that GlyHCl further retards the oxidation of SnI$_2$. The color of the solutions containing SnF$_2$ remained unchanged, even after 30 h. Hence, GlyHCl retards air oxidation of SnI$_2$ in DMF and DMSO, but the stabilizing effect is smaller than that of SnF$_2$.

Film crystallization and morphology also affect the stability and device performance. The perovskite films prepared using varying amounts of GlyHCl were analyzed using scanning electron microscopy (SEM) (**Figure 2**a and Figure S7, Supporting Information). The control film appeared to be a smooth and closed layer with a mean grain size of $\approx$450 nm (Figure S8, Supporting Information). Additionally, a white needle-shaped residue was present on top of the film, most likely PbI$_2$, matching the observed peak at 12.7° in the X-ray diffraction (XRD) measurements (Figure S9, Supporting Information). Upon the addition of GlyHCl, the white needles were no longer observed and the XRD peak of PbI$_2$ at 12.7° decreased to noise level. Besides the removal of the excess PbI$_2$, the amount of GlyHCl used also influenced the grain size distribution (Figure S8, Supporting Information). The mean grain size increased to $\approx$570 nm with the addition of 1–2 mol% GlyHCl and rose further to 680 and 710 nm for the perovskite films with 4 and 10 mol%, respectively. The spread in grain sizes also increased with GlyHCl concentration, for example, the 1 mol% sample has a more Gaussian size distribution with most grains having a similar size as the mean. However, the 2 mol% sample also has a large population of smaller grains between 150 and 400 nm, as well as larger grains above 800 nm (Figure S8, Supporting Information). Hereby, the smaller grains can fit in the cavities around the larger grains thereby forming a compact layer. For the 4 mol% sample, a large increase in the population of the larger grains is visible. Whereas for the 10 mol% sample the distribution shrinks caused by the absence of the smaller grains, instead pinholes appeared in the layer (Figure 2a). Besides these pinholes, large, almost amorphous-looking patches were observed on this film, possibly an excess of GlyHCl ending up at the top surface of the perovskite (Figure 2a). To determine whether the GlyHCl could also reach the top surface of the perovskite, XPS was conducted. A clear Cl 2p signal appeared for the films processed with GlyHCl and the signal increased with higher concentrations (Figure S10a, Supporting Information). Simultaneously, the 532 eV oxygen peak related to the carboxylic acid group emerged (Figure S10b, Supporting Information), confirming that both moieties could move to the top interface.

Additionally, XRD revealed the characteristic Pb–Sn perovskite diffraction peaks at 14.3°, 20.1°, 24.7°, 28.5°, 31.9°, 35.1°, 40.7°, 43.2°, 48.0°, 50.2°, and 52.4° related to the (100), (110), (111), (200), (210), (211), (220), (300), (310), (222), and (400) orientations, respectively, for all films (Figure S9, Supporting Information). Small variations in the peak positions can be seen. For example, the (100) peak shifts to slightly higher angle at 1 mol% GlyHCl and then to intermediate angles for 2, 4, and
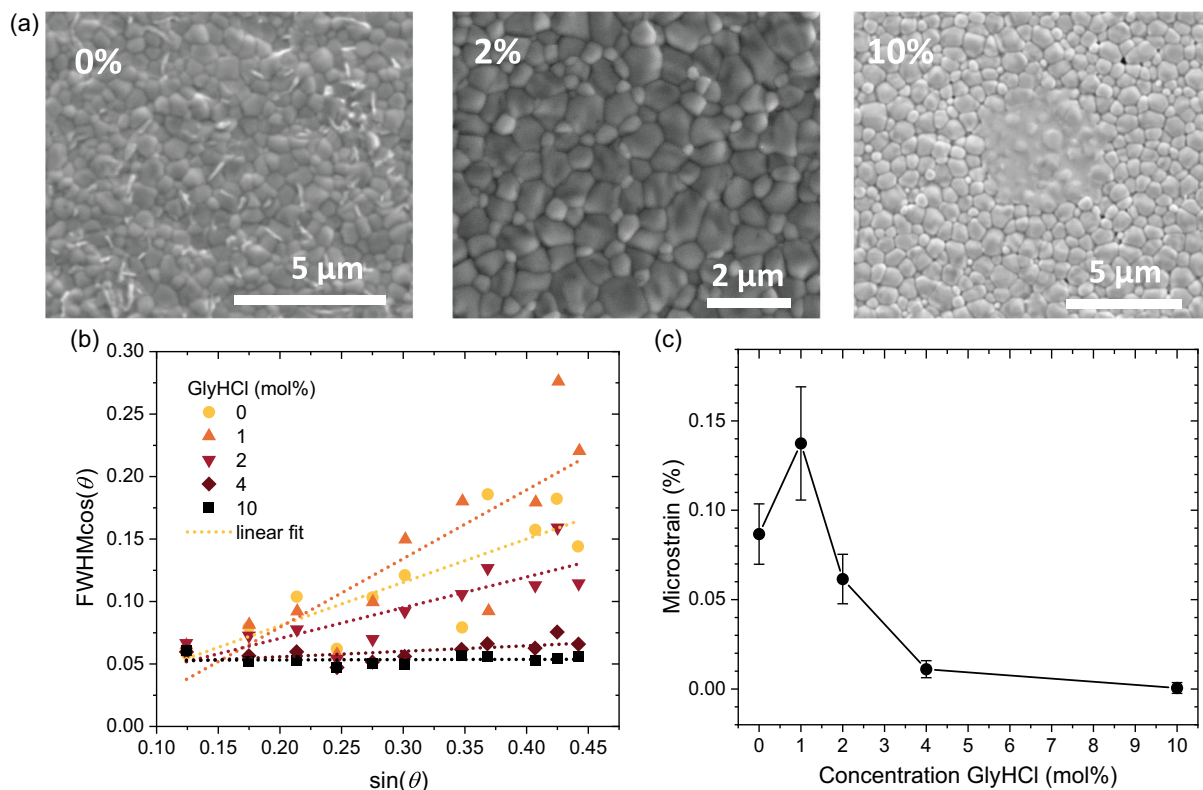
Figure 2. a) SEM images of $Cs_{0.1}FA_{0.6}MA_{0.3}Pb_{0.5}Sn_{0.5}I_3$ films, processed with 2 mol% GuaSCN, 5 mol% SnF_2, and 0, 2, or 10 mol% GlyHCl. b) Williamson–Hall (W–H) plot of $Cs_{0.1}FA_{0.6}MA_{0.3}Pb_{0.5}Sn_{0.5}I_3$ films, processed with 2 mol% GuaSCN, 5 mol% SnF_2, and 0, 1, 2, 4, or 10 mol% GlyHCl. c) The micro-strain obtained from the W–H plot for the $Cs_{0.1}FA_{0.6}MA_{0.3}Pb_{0.5}Sn_{0.5}I_3$ films, processed with 2 mol% GuaSCN, 5 mol% SnF_2, and 0, 1, 2, 4, or 10 mol% GlyHCl.

10 mol%. This indicates that GlyHCl affects the crystallization, but we cannot conclude that it is incorporated in the lattice. Concomitantly, the bandgap, determined from the second derivative of the EQE spectrum (Figure S4f, Supporting Information), varies between 1.272 and 1.257 eV with the GlyHCl concentration but not in a monotonous fashion. Hence, GlyHCl influences the structural and electronic properties in a subtle way.

To assess the influence of GlyHCl on the bulk structure of the perovskite film in more detail, a Williamson-Hall (W–H) analysis was conducted. This method evaluates the micro-strain by the broadening of the XRD peaks with increasing 2θ angles (Figure S11, Supporting Information). Identifying strain in the perovskite lattice is important due to its detrimental impact on the optoelectronic properties and stability of perovskite films.[35] Figure 2b shows the W–H plot of $FWHMcos(\theta)$ (FWHM is full-width at half maximum) as a function of $sin(\theta)$. Linear fits have been applied and the micro-strain was obtained from the slope. All samples portray a positive slope, which indicates the presence of tensile strain. With the addition of GlyHCl, a pronounced effect is observed as the micro-strain notably decreases from 0.09% to 0.0005% (Figure 2c). Interestingly, the data points corresponding to the (100) and (200) reflections overlap in the W–H plot. This suggests that the strain effect is not isotropic and the $h00$ direction can be associated with a form of strain release, independent of the presence of GlyHCl.

To investigate the effect of GlyHCl on the non-radiative recombination losses and V_{OC}, the quasi-Fermi level splitting (QFLS) was measured by recording the absolute photoluminescence photon flux of the perovskite films with and without GlyHCl. The QFLS values for the neat perovskite films on glass with 0, 1, 2, and 4 mol% GlyHCl are shown in **Figure 3**a. Without GlyHCl the film showed a QFLS of 886 meV, representing 88.6% of the radiative limit for a 1.27 eV bandgap semiconductor (1000 meV). For perovskite films prepared with 1 and 2 mol% GlyHCl, the non-radiative losses were reduced and the QFLS improved to 898 and 900 meV, achieving 90.0% of the radiative limit. Hence, the use of a small amount of GlyHCl increased the quality of the bulk perovskite. However, when the concentration of the GlyHCl was increased to 4 mol%, the QFLS dropped to a value of 875 meV, so 11 meV below the control sample, indicating that an excess of GlyHCl creates defects that cause non-radiative recombination.

To evaluate the effect of GlyHCl on the complete device stack and to determine which interfaces suppress the V_{OC}, an interfacial loss analysis was performed by measuring the QFLS of the perovskite film in combination with the ETL, HTL, or both (Figure 3b). For the HTL/perovskite interface, perovskite films were prepared on ITO/PEDOT:PSS covered glass substrates. Independent of the GlyHCl concentration used, the QFLS of the perovskite dropped by ≈40 meV when processed on top of
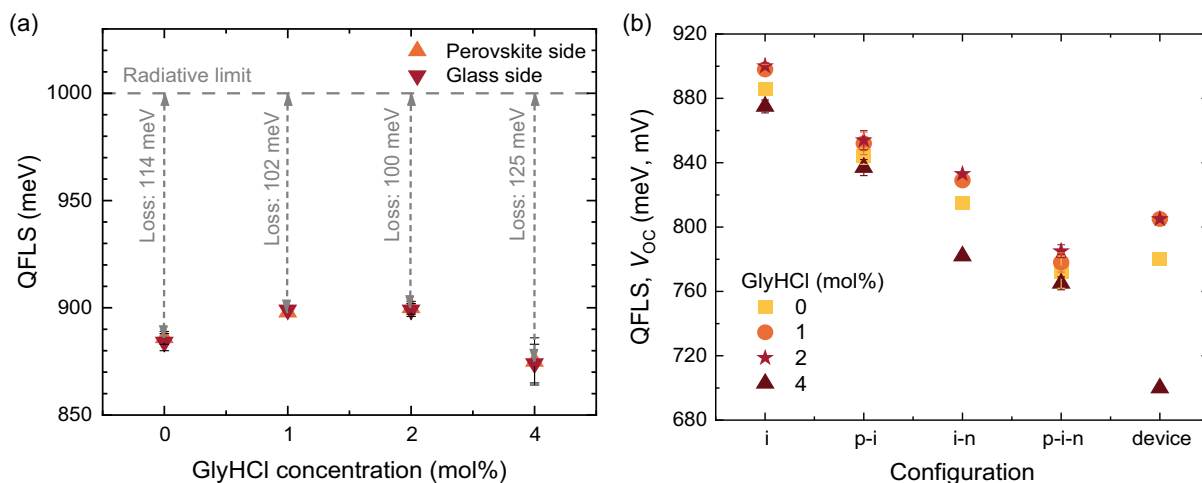
Figure 3. a) The QFLS of $Cs_{0.1}FA_{0.6}MA_{0.3}Pb_{0.5}Sn_{0.5}I_3$ films, processed with 2 mol% GuaSCN, 5 mol% SnF_2, and 0, 1, 2, or 4 mol% GlyHCl. The absolute photoluminescence photon flux was measured both from the glass and perovskite film side. The radiative limit of a perovskite with a bandgap of 1.27 eV is 1000 meV and the QFLS losses per film are stated. b) The QFLS and V_{OC} obtained for perovskite films processed with 2 mol% GuaSCN, 5 mol% SnF_2, and 0, 1, 2, or 4 mol% GlyHCl for four configurations: glass/perovskite (i), glass/ITO/PEDOT:PSS/perovskite (p-i), glass/perovskite/C_{60} (i-n), and glass/ITO/PEDOT:PSS/perovskite/C_{60} (p-i-n) together with the actual V_{OC} (device).

the PEDOT:PSS layer compared to samples on glass. Because this drop is not affected by the GlyHCl concentration, an interaction between GlyHCl and PEDOT:PSS seems unlikely. It rather suggests that the GlyHCl improves the quality of the perovskite bulk independent of the surface on which the perovskite precursor solution is deposited. This may also explain how GlyHCl can benefit the production of HTL-free Pb–Sn perovskites.[16] An almost doubled decrease in QFLS was incurred when C_{60} was evaporated on top of the perovskite film on glass. The 0, 1, and 2 mol% devices featured QFLS losses of 71, 69, and 67 meV, respectively, again suggesting that there is no significant effect of GlyHCl on the interfacial losses when low concentrations are used. Notably, with 4 mol% GlyHCl, a noticeably larger loss of 93 meV was found. Even though no amorphous patches were observed with SEM for this concentration, XPS did show that relatively higher amounts of chloride and carboxylic acid were present at the top surface (Figure S10, Supporting Information). An excess of GlyHCl could cause defect states and promote recombination. This could lead to a decrease in the V_{OC} of the device. When both HTL and ETL were present, the 2 mol% GlyHCl remained achieving the highest QFLS. When comparing the V_{OC} of the devices to the QFLS, there is a small increase for all samples, except for the devices processed with 4 mol% GlyHCl. The excess of GlyHCl on top could hinder charge collection at the Ag electrode, lowering V_{OC}.

Light intensity-dependent measurements of the QFLS were performed to obtain a further understanding of the non-radiative losses in the perovskite bulk and at the interfaces without suffering from charge transport losses.[36,37] From the slope of the QFLS against the light intensity, the ideality factor (n_{ID}) can be determined. The ideality factor is related to the dominant charge recombination mechanism.[38] **Figure 4**a displays the QFLS of the neat perovskite films on glass, measured over a light intensity range of 0.002–2 sun equivalents and the linear fits to determine n_{ID}. For the films processed with 0, 1, and 2 mol%

GlyHCl, n_{ID} varies around 1.26 ± 0.07, with the lowest value (1.19) found for 1 mol% GlyHCl. In combination with a high QFLS, an n_{ID} closer to 1 signifies less non-radiative trap-assisted (Shockley–Read–Hall, SRH) recombination losses and more radiative band-to-band recombination. Increasing the GlyHCl concentration to 4 mol%, resulted in a distinct increase of n_{ID} to 1.47 and loss of QFLS, suggesting an increasing contribution of SRH recombination.

Light intensity-dependent measurements were also performed on perovskite films combined with the HTL (PEDOT:PSS) and/or ETL (C_{60}) (Figure S12, Supporting Information). The ideality factors are shown in Figure 4c, Figure S12 and Table S7 (Supporting Information). When the perovskite film was spin-coated on PEDOT:PSS, the QFLS dropped (Figure 3b), but n_{ID} changed by either decreasing slightly (2 mol%), remaining constant (1 and 4 mol%), or increasing slightly (0 mol%). The decrease of n_{ID} for the 2 mol% sample does not necessarily evidence more band-to-band recombination, because the simultaneous loss of QFLS and n_{ID} is rather explained by increased surface recombination.[38] With the evaporation of a thin C_{60} layer on the neat perovskite, the n_{ID} values changed to 1.35 ± 0.01 with a concomitant drop of QFLS. A similar value (1.31 ± 0.03) is found for the complete p-i-n stacks when using 0, 1, and 2 mol% with an additional loss in QFLS compared to the i-n configurations. For the 4 mol%, the ideality factor increased to 1.49 but the drop in QFLS compared to i-n was less. Interpreting these n_{ID} values in terms of a dominant recombination mechanism is not possible at this stage, but the drop in QFLS when going from either p-i or i-n to the p-i-n configuration indicates that the interfaces of the perovskite with both the HTL and the ETL significantly contribute to the non-radiative recombination at open-circuit.

The QFLS-light intensity data were converted into pseudo $J–V$ curves by using the proportionality of the photocurrent density and light intensity and taking the QFLS as the voltage.[37] Using
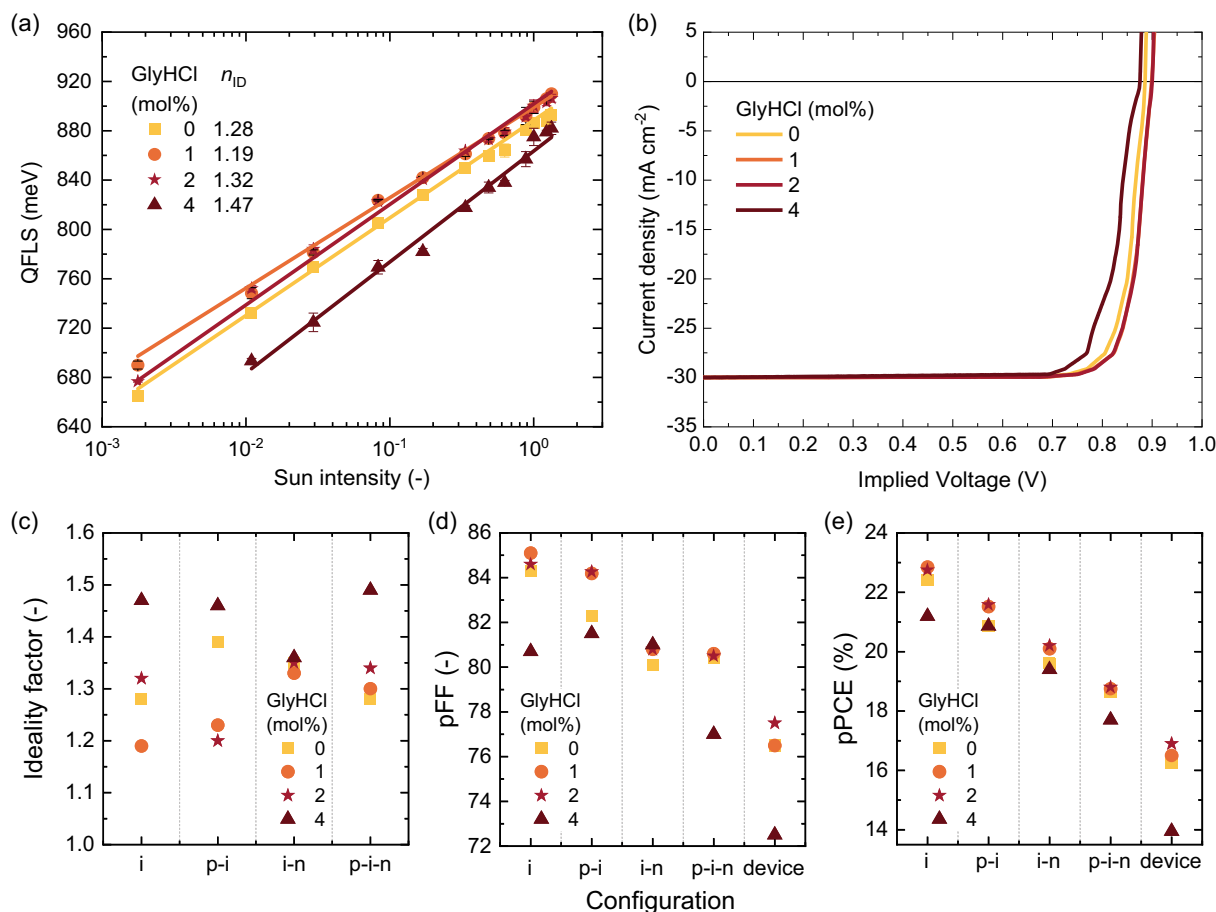
Figure 4. a) The QFLS obtained from the light intensity-dependent absolute photoluminescence measurement on perovskite films on glass processed with 2 mol% GuaSCN, 5 mol% SnF_2, and 0, 1, 2, or 4 mol% GlyHCl measured between 0.002 and 2 sun equivalents. The legend shows the ideality factors obtained from linear fits (solid lines). b) Pseudo J–V curves determined from the bulk perovskite light intensity-dependent measurements of the bulk perovskite films. Note that the data for 1 and 2 mol% GlyHCl overlap in the graph. c) Ideality factor, d) pseudo fill factor (pFF), and e) pseudo power conversion efficiency (pPCE) obtained from the light intensity-dependent measurements of the bulk perovskite films with 0, 1, 2, and 4 mol% GlyHCl per configuration: neat perovskite film (i), HTL with perovskite (p-i), perovskite with ETL (i-n), p-i-n stack. These values are compared to the FF and PCE obtained from the J–V sweeps of the full device.

the pseudo J–V data for different GlyHCl concentrations on glass (Figure 4b), the pseudo fill factor (pFF, Figure 4d) and pseudo power conversion efficiency (pPCE, Figure 4e) can be determined. For the neat perovskite films on glass, there is an opposite relation between the n_{ID} and the pFF. Films with the lowest n_{ID} yielded the highest pFF of 84–85%. Combined with the high QFLS of the 1 and 2 mol% GlyHCl films, a pPCE of 22.7% is found. The small changes that occur in n_{ID} when applying the perovskite layer on PEDOT:PSS, that is, a p-i configuration, leave the pFF high for films processed with 1 or 2 mol% GlyHCl, but the loss in QFLS still reduces the pPCE. In contrast, when C_{60} is applied on top of the perovskite, that is, an i-n configuration, the pFF dropped more for these concentrations. Although no further loss in pFF is observed in the PEDOT:PSS/perovskite/C_{60} (p-i-n) stack (for 0, 1, and 2 mol%), the pPCE shows a downward trend because the QFLS continues to decrease (Figure 3b). These results stress the importance and need for additional passivation of the interface of the perovskite with the charge transport layers.

When the full p-i-n stack is compared to the device, an additional loss in performance is observed due to the collection and transport losses neglected in these measurements but those do occur when operating the solar cells. The analogy in the reduction of the PCEs found for the four different samples demonstrates again that GlyHCl impacts the bulk properties rather than those of the surface.

Time-resolved microwave conductivity (TRMC) measurements were performed on neat perovskite films to investigate the influence of GlyHCl on the recombination kinetics and lifetime of light-induced, excess charges. To generate mobile charges, a nanosecond laser pulse with a wavelength of 800 nm was employed with repetition rate of 10 Hz. The initial rise in the intensity-normalized photoconductance (ΔG) signal is due to the generation of free charges (**Figure 5**a). Assuming constant electron and hole mobilities as a function of photoconductance, the decay characteristics provide insight into the recombination or immobilization mechanisms.[39] Figure 5a
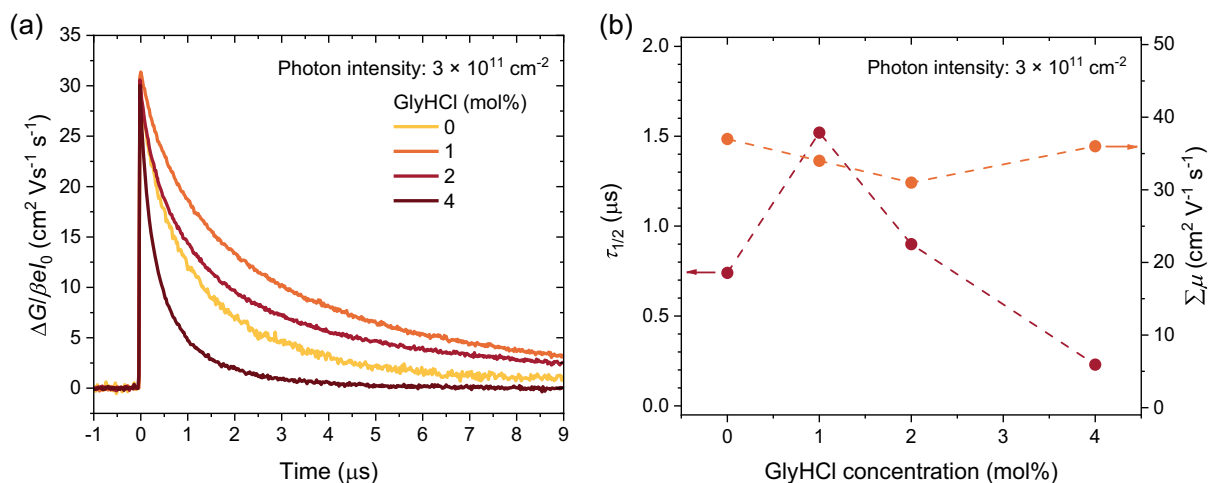
Figure 5. a) Time-resolved microwave conductivity (TRMC) signals on perovskite thin films processed with 2 mol% GuaSCN, 5 mol% SnF_2, and 0, 1, 2, or 4 mol% GlyHCl. b) Half-lifetimes (left axis) and the sum of electron and hole mobility (right axis) as a function of the GlyHCl concentration in the precursor solution. These values were extracted from the TRMC data.

presents the TRMC traces of the perovskite films processed with varying amounts of GlyHCl at a laser intensity of 3×10^{11} photons per pulse per cm^2. The maximum photoconductance signal is a measure of the product of the yield and the sum of electron and hole mobilities ($\Sigma\mu$) in the sample. Assuming a yield of 1, all samples exhibited mobilities exceeding $30 \, cm^2 \, V^{-1} \, s^{-1}$, comparable to previously reported values.[40] Hence, the charge mobilities within the perovskite grains are very similar and largely independent of the use of GlyHCl as an additive. When the GlyHCl concentration increases from 0 to 1 mol%, the carrier half-lifetime ($\tau_{1/2}$) doubles from 0.7 to 1.5 µs (Figure 5b) at the used laser intensity. However, at higher GlyHCl concentrations of 2 and 4 mol%, the TRMC traces showed shorter decay times, suggesting an optimal concentration range. Longer lifetimes indicate that for the 1 mol% GlyHCl perovskite samples less undesired recombination occurs, which is in accordance with the actual V_{OC} of the devices with different GlyHCl concentrations.[41]

3. Conclusion

In this work, we show that glycine hydrochloride has a beneficial effect on the crystallization, photovoltaic performance and stability of narrow-bandgap mixed Pb–Sn perovskites. Small amounts of GlyHCl (1–2 mol%) cause an increase in the V_{OC} and FF of the devices, achieving values of 0.81 V and 78%, yielding a PCE of 17.4%. A concentration of 2 mol% seems to be the optimum in terms of stability because the cells show almost no performance loss when tracking the current at the maximum point voltage or the open-circuit voltage during continued illumination. The higher device performance when using 1 or 2 mol% of GlyHCl in the precursor solution are related to the ability of GlyHCl to retard the oxidation of Sn^{2+}, improve the grain size distribution causing a smoother and more compact layer, reduce non-radiative recombination, and slow the recombination of charge carriers. However, when a larger amount (4 or 10 mol%) of GlyHCl is added, an excess seems to accumulate at the

top of the perovskite surface, introducing defect states and hindering charge collection. TRMC measurements show that the charge mobility is largely independent of the GlyHCl concentration but the lifetime reaches a maximum when using 1 mol%. Absolute photoluminescence measurements indicate that GlyHCl enhances the quality of the bulk of the narrow-bandgap perovskite but that further passivation of the film and transport layers is required to enhance performance. Non-radiative recombination at the perovskite–ETL interface seems most prominent in our experiments.

4. Experimental Section

Materials: All materials were used as received without further purification and stored under nitrogen. Formamidinium iodide (FAI, >99.99%) and methylammonium iodide (MAI, >99.99%) were purchased from Greatcell Solar Materials. Lead(II) iodide (PbI_2, 99.99% trace metal basis) and guanidine thiocyanate (GuaSCN, >99.0%) were purchased from TCI Chemicals. Poly(3,4-ethylenedioxythiophene): poly(styrene sulfonate) (PEDOT:PSS, PVP Al 4083) was purchased from Heraeus Clevios. Anhydrous tin(II) iodide beads (SnI_2, 99.99% trace metals basis), tin(II) fluoride (SnF_2, 99%), anhydrous cesium iodide beads (CsI, 99.999% trace metals basis), glycine hydrochloride (GlyHCl, ≥99% (HPLC)), ammonium thiocyanate (ACS reagent, ≥97.5%), anhydrous *N*,*N*-dimethylformamide (DMF, 99.8%), anhydrous dimethyl sulfoxide (DMSO, ≥99.9%), and anhydrous chlorobenzene (CB, 99.8%) were purchased from Sigma-Aldrich. Bathocuproine (BCP, >99.5%) was purchased from Lumtec and the C_{60} fullerene (99.99%) from SES Research.

Precursor Solution Preparation: The perovskite precursor solution for a perovskite film with a nominal composition of $Cs_{0.1}FA_{0.6}MA_{0.3}Pb_{0.5}Sn_{0.5}I_3$ was made by dissolving 0.9 M PbI_2, 0.9 M SnI_2, 0.18 M CsI, 1.08 M FAI, and 0.54 M MAI in a DMF/DMSO mixture with a volume ratio of 3:1. Additionally, 0.045 M SnF_2 and 0.018 M NH_4SCN were added. For the devices with different GlyHCl concentrations, separate precursor solutions were made with either 0, 0.5, 1, 2, 4, or 10 mol% of GlyHCl relative to the total metal (PbI_2 and SnI_2) concentration. The solutions were stirred for 40 min at 45 °C. After cooling to room temperature, the solutions were filtered using a 0.22 µm polytetrafluoroethylene syringe filter. All solutions were prepared in a nitrogen environment. In the renewed recipe, the NH_4SCN was replaced with 0.036 M GuaSCN.

Film Fabrication: For the spin-coating of perovskite films on glass, 200 µL of the precursor solution was deposited on the substrate and the first spinning step was started for 10 s at 1000 rpm with an acceleration of 200 rpm s^{-1}, followed by a second step of 40 s at 4000 rpm with an acceleration of 1000 rpm s^{-1}. To quench the perovskite, 400 µL chlorobenzene was deposited on the film 43 s after the start of the spinning. Next, the film was annealed at a hotplate of 100 °C for 10 min followed by 10 min at 65 °C. For the renewed recipe, the chlorobenzene was deposited after 51 s instead of 43 s and the films were first annealed at a hotplate of 65 °C for 10 min followed by 10 min at 100 °C.

Device Fabrication: Patterned-ITO glass substrates were sonicated in acetone, scrubbed clean in soapy water, sonicated in soapy water, flushed with demi-water, and sonicated in 2-propanol. Before use, the substrates had a 30 min UV-ozone treatment. The PEDOT:PSS HTL was deposited in ambient air. The aqueous dispersion was filtered using a 0.45 µm polyvinylidene difluoride filter and 150 µL was pipetted onto the substrate. The layer was spin-coated using a first spinning step of 10 s at 500 rpm with an acceleration of 20 000 rpm s^{-1} and followed by 30 s at 4000 rpm with a ramp of 20 000 rpm s^{-1}. The films were annealed for 20 min at 140 °C before transferring them to the N$_2$ glovebox where they had a second round of annealing of 30 min at 140 °C. After cooling to room temperature, the perovskite film was spin-coated with the one-step anti-solvent method in the glove box as explained earlier. For the ETL, 20 nm C$_{60}$ and 8 nm BCP were thermally evaporated with a rate of 0.2 Å s^{-1} under high vacuum (2–6 × 10^{-7} mbar). Ag was thermally evaporated as the top electrode, using an initial rate of 1 Å s^{-1} increasing to 3 Å s^{-1} to reach the target thickness of 100 nm.

Photovoltaic Performance Characterization: The J–V and EQE measurements were taken under dry and oxygen-free nitrogen atmosphere (<1 ppm O$_2$ and <1 ppm H$_2$O). For the J–V measurements, a tungsten-halogen lamp (100 mW cm^{-2}) was used with a UV filter (Schott GG385) and a daylight filter (Hoya LB120) to simulate the AM 1.5 G solar spectrum. A shadow mask with 0.0676 and 0.1296 cm^2 aperture sizes was used to define the illuminated active area. J–V characteristics of the solar cells were measured with a Keithley 2400 SMU in involved sweeping the applied voltage (with no pre-biasing) from +1.0 to −0.5 V for a backward scan or from −0.5 to +1.0 V for a forward scan in steps of 0.01 V at a scan rate of 0.25 V s^{-1}. The same setup was used for stability testing. To measure EQE, the cells were contacted in a nitrogen-filled container. A 50 W tungsten-halogen lamp was used as light source. The light was chopped at 158 Hz before passing into a monochromator (Oriel, Cornerstone 130). A reference silicon detector was used to calibrate the current from the cell which was fed into a current pre-amplifier (Stanford Research, SR 570). The resulting voltage was measured using a lock-in amplifier (Stanford Research, SR 830). A green (Thorlabs, M530L3) LED was used as a light bias to generate ≈1-sun equivalent illumination intensity. Integration of the EQE with the AM1.5G spectrum afforded estimates of J_{SC}.

Scanning Electron Microscopy: SEM images were collected with a FEI Quanta 3D FEG microscope (5 keV electron beam, secondary electron detector) and a PhenomProX (5 keV electron beam, secondary electron detector).

Thickness and Roughness: Surface profilometry was performed with a Veeco Dektak 150.

X-Ray Diffraction: XRD was recorded in the Bragg-Brentano configuration on a Bruker D8 Advance diffractometer in ambient air. A Cu source ($\lambda_{K\alpha1}$ = 1.5406 Å) was used and the measurements were done in the 2θ range of 5–70° with a step size of 0.005° and a collection time of 0.1 s. For the W–H analysis, the perovskite peaks ((100), (110), (111), (200), (210), (211), (220), (300), (310), (222), and (400)) were measured in smaller ranges (13–15°, 19–21°, 23.5–25.5°, 27.3–29.3°, 30.7–32.7°, 33.9–35.9°, 39.7–41.7°, 42.3–44.3°, 47–49°, 49.4–51.4°, and 51.5–53.5°, respectively) with a step size of 0.001° and a collection time of 0.25 s. To account for the contribution of Kα2 reflections, the exact reflection angle and FWHM were obtained by fitting all the peaks with two Voigt functions. Subsequently, the W–H plot was constructed by plotting the FWHMcos(θ) against sin(θ), and a linear fit was applied to determine the strain, following Equation (1). Here, ε is the micro-strain in %, k is the shape factor (here taken 0.9), λ is the wavelength of the Cu source, and D is the crystallite size.

$$FWHM \cos(\theta) = 4\varepsilon \sin(\theta) + \frac{k\lambda}{D} \tag{1}$$

X-Ray Photoelectron Spectroscopy: XPS measurements were performed using a Thermo-Scientific K-Alpha with a 180° double-focusing hemispherical analyzer and a 128-channel detector. Monochromatic Al Kα (1486.6 eV) radiation was used, and the X-ray spot size was 400 µm. For the surface analysis, a survey spectrum was first measured for 12 scans (dwell time of 20 ms) with a pass energy of 200 eV. High-resolution scans (30 times, dwell time of 50 ms) of each element were conducted with a pass energy of 50 eV. The depth-profile measurement was performed in etching mode with an ion energy of 500 eV and low current (sputter rate estimate of 0.05 nm s^{-1}). Each etch cycle had a duration of 30 sand 150 total levels were measured.

Quasi-Fermi Level Splitting: The sample is illuminated using a 455 nm Thorlabs M455F3 or 470 nm Thorlabs M470F3 fiber-coupled LED. The light passes through an in-fiber filter holder containing an Edmund Optics 550 nm short-pass filter before entering an integrating sphere (Avantes AvaSphere-30-REFL). The PL emission from the sample is collected through an optical fiber mounted to the side of the sphere and is passed through an in-fiber filter holder with an Edmund Optics 550 nm long-pass filter before it is collected by a spectrometer (Avantes AvaSpec-HSC1024X58TEC-EVO). The setup was calibrated using an irradiance calibrated halogen light source (Avantes AVALIGHT-HAL-CAL-ISP30-MINI).To match the conditions for open-circuit voltage under AM1.5 illumination, the intensity of the LED was adjusted to 1-sun equivalent intensity by matching to the short-circuit current density of the perovskite solar cell. The spectral photon flux (φ_{PL}) was obtained after a Jacobian transformation. The relation between QFLS ($\Delta\mu$) and φ_{PL} is given by the generalized Planck equation:

$$\varphi_{PL}(E) = \frac{1}{4\pi^2\hbar^3c^2} \frac{a(E)E^2}{\exp\left(\frac{E-\Delta\mu}{k_BT}\right) - 1} \tag{2}$$

where $a(E)$ is the photon energy-dependent absorptivity, the reduced Planck constant, c the speed of light in vacuum, k_B the Boltzmann constant, and T the temperature.[42,43] $a(E)$ is assumed to be unity for photon energies sufficiently larger than the optical bandgap. $\Delta\mu$ was determined from φ_{PL} via a nonlinear least squares fit. For the light intensity-dependence the excitation photon flux in the experiment was adjusted and measured with a power meter (Ophir Nova). This intensity was simultaneously checked with a perovskite solar cell measured in an in-house build sample holder.

Time-Resolved Microwave Conductivity: TRMC was performed to study the photoconductance of samples as a function of time. This technique relies on the interaction between microwaves and light-induced excess carriers in the materials. For this measurement, quartz substrates were covered with the neat perovskite film containing the varying GlyHCl concentrations. The samples were placed inside a sealed measurement cell inside an N$_2$-filled glovebox to prevent any exposure to ambient conditions. Charge carriers were generated using a laser pulse (repetition rate 10 Hz) with an excitation wavelength of 800 nm. The reduction of reflected microwave power ($\Delta P(t)/P$) is related to a change in conductance ($\Delta G(t)$) using the sensitivity factor K:

$$\frac{\Delta P(t)}{P} = -K\Delta G(t) \tag{3}$$

The TRMC signal is expressed in the product of mobility ($\mu_e + \mu_h$) and charge carrier yield φ, which was calculated from the maximum change in photoconductance ΔG_{max}:

$$\varphi(\mu_e + \mu_h) = \frac{\Delta G_{max}}{I_0 e\beta} \tag{4}$$

where I_0 is the laser intensity in number of photons per unit area per pulse, e is the elementary charge, and β is a geometrical factor accounting for the ratio of the inner dimensions of the cavity cell.

[1] J. Tong, Q. Jiang, A. J. Ferguson, A. F. Palmstrom, X. Wang, J. Hao, S. P. Dunfield, A. E. Louks, S. P. Harvey, C. Li, H. Lu, R. M. France, S. A. Johnson, F. Zhang, M. Yang, J. F. Geisz, M. D. McGehee, M. C. Beard, Y. Yan, D. Kuciauskas, J. J. Berry, K. Zhu, *Nat. Energy* **2022**, *7*, 642.

[2] K. Xiao, R. Lin, Q. Han, Y. Hou, Z. Qin, H. T. Nguyen, J. Wen, M. Wei, V. Yeddu, M. I. Saidaminov, Y. Gao, X. Luo, Y. Wang, H. Gao, C. Zhang, J. Xu, J. Zhu, E. H. Sargent, H. Tan, *Nat. Energy* **2020**, *5*, 870.

[3] J. Luo, R. He, H. Lai, C. Chen, J. Zhu, Y. Xu, F. Yao, T. Ma, Y. Luo, Z. Yi, Y. Jiang, Z. Gao, J. Wang, W. Wang, H. Huang, Y. Wang, S. Ren, Q. Lin, C. Wang, F. Fu, D. Zhao, J. Luo, R. He, C. Chen, J. Zhu, Y. Xu, Y. Luo, Z. Yi, Y. Jiang, Z. Gao, et al., *Adv. Mater.* **2023**, *35*, 2300352.

[4] K. Datta, J. Wang, D. Zhang, V. Zardetto, W. H. M. Remmerswaal, C. H. L. Weijtens, M. M. Wienk, R. A. J. Janssen, *Adv. Mater.* **2022**, *34*, 2110053.

[5] F. Hao, C. C. Stoumpos, P. Guo, N. Zhou, T. J. Marks, R. P. H. Chang, M. G. Kanatzidis, *J. Am. Chem. Soc.* **2015**, *137*, 11445.

[6] W. Ke, C. C. Stoumpos, M. G. Kanatzidis, *Adv. Mater.* **2019**, *31*, 1803230.

[7] X. Jiang, H. Li, Q. Zhou, Q. Wei, M. Wei, L. Jiang, Z. Wang, Z. Peng, F. Wang, Z. Zang, K. Xu, Y. Hou, S. Teale, W. Zhou, R. Si, X. Gao, E. H. Sargent, Z. Ning, *J. Am. Chem. Soc.* **2021**, *143*, 10970.

[8] B. Li, B. Chang, L. Pan, Z. Li, L. Fu, Z. He, L. Yin, *ACS Energy Lett.* **2020**, *5*, 3752.

[9] Z. Zhang, J. Liang, Y. Zheng, X. Wu, J. Wang, Y. Huang, Y. Yang, Z. Zhou, L. Wang, L. Kong, K. M. Reddy, C. Qin, C. C. Chen, *J. Mater. Chem. A* **2021**, *9*, 17830.

[10] H. L. Zhu, J. Xiao, J. Mao, H. Zhang, Y. Zhao, W. C. H. Choy, *Adv. Funct. Mater.* **2017**, *27*, 1605469.

[11] L. Lanzetta, T. Webb, N. Zibouche, X. Liang, D. Ding, G. Min, R. J. E. Westbrook, B. Gaggio, T. J. Macdonald, M. S. Islam, S. A. Haque, *Nat. Commun.* **2021**, *12*, 2853.

[12] X. Ding, M. Yan, C. Chen, M. Zhai, H. Wang, Y. Tian, L. Wang, L. Sun, M. Cheng, *Angew. Chem. Int. Ed.* **2024**, *63*, e202317676.

[13] C. T. Lin, F. De Rossi, J. Kim, J. Baker, J. Ngiam, B. Xu, S. Pont, N. Aristidou, S. A. Haque, T. Watson, M. A. McLachlan, J. R. Durrant, *J. Mater. Chem. A* **2019**, *7*, 3006.

[14] C. T. Lin, W. Xu, T. J. Macdonald, J. Ngiam, J. H. Kim, T. Du, S. Xu, P. S. Tuladhar, H. Kang, K. Lee, J. R. Durrant, M. A. Mclachlan, *ACS Appl. Mater. Interfaces* **2021**, *13*, 43505.

[15] H. Yuan, Z. Zhang, T. Guo, L. Yu, Z. Deng, R. Zhao, J. Zhang, Y. Zhu, *J. Alloys Compd.* **2021**, *876*, 160140.

[16] H. Kim, J. W. Lee, G. R. Han, Y. J. Kim, S. H. Kim, S. K. Kim, S. K. Kwak, J. H. Oh, *Adv. Funct. Mater.* **2022**, *32*, 2110069.

[17] S. Hu, K. Otsuka, R. Murdey, T. Nakamura, M. A. Truong, T. Yamada, T. Handa, K. Matsuda, K. Nakano, A. Sato, K. Marumoto, K. Tajima, Y. Kanemitsu, A. Wakamiya, *Energy Environ. Sci.* **2022**, *15*, 2096.

[18] H. Chen, A. Maxwell, C. Li, S. Teale, B. Chen, T. Zhu, E. Ugur, G. Harrison, L. Grater, J. Wang, Z. Wang, L. Zeng, S. M. Park, L. Chen, P. Serles, R. A. Awni, B. Subedi, X. Zheng, C. Xiao, N. J. Podraza, T. Filleter, C. Liu, Y. Yang, J. M. Luther, S. De Wolf, M. G. Kanatzidis, Y. Yan, E. H. Sargent, *Nature* **2023**, *613*, 676.

[19] H. Zheng, W. Wu, H. Xu, F. Zheng, G. Liu, X. Pan, Q. Chen, *Adv. Funct. Mater.* **2020**, *30*, 2000034.

[20] H. Zhang, M. Hou, Y. Xia, Q. Wei, Z. Wang, Y. Cheng, Y. Chen, W. Huang, *J. Mater. Chem. A* **2018**, *6*, 9264.

[21] S. Yang, W. Liu, L. Zuo, X. Zhang, T. Ye, J. Chen, C. Z. Li, G. Wu, H. Chen, *J. Mater. Chem. A* **2016**, *4*, 9430.

[22] J. Pascual, M. Flatken, R. Félix, G. Li, S. H. Turren-Cruz, M. H. Aldamasy, C. Hartmann, M. Li, D. Di Girolamo, G. Nasti, E. Hüsam, R. G. Wilks, A. Dallmann, M. Bär, A. Hoell, A. Abate, *Angew. Chem., Int. Ed.* **2021**, *60*, 21583.

[23] Q. Chen, J. Luo, R. He, H. Lai, S. Ren, Y. Jiang, Z. Wan, W. Wang, X. Hao, Y. Wang, J. Zhang, I. Constantinou, C. Wang, L. Wu, F. Fu, D. Zhao, *Adv. Energy Mater.* **2021**, *11*, 2101045.

[24] S. Gupta, D. Cahen, G. Hodes, *J. Phys. Chem. C* **2018**, *122*, 13926.

[25] K. J. Savill, A. M. Ulatowski, M. D. Farrar, M. B. Johnston, H. J. Snaith, L. M. Herz, *Adv. Funct. Mater.* **2020**, *30*, 2005594.

[26] J. Zou, W. Liu, W. Deng, G. Lei, S. Zeng, J. Xiong, H. Gu, Z. Hu, X. Wang, J. Li, *Electrochim. Acta* **2018**, *291*, 297.

[27] S. Zhong, Z. Li, C. Zheng, X. Luo, J. Gao, X. Lu, X. Gao, L. Shui, S. Wu, J. M. Liu, *Sol. RRL* **2022**, *6*, 2200088.

[28] M. I. Saidaminov, J. Kim, A. Jain, R. Quintero-Bermudez, H. Tan, G. Long, F. Tan, A. Johnston, Y. Zhao, O. Voznyy, E. H. Sargent, *Nat. Energy* **2018**, *3*, 648.

[29] X. Xu, C. C. Chueh, Z. Yang, A. Rajagopal, J. Xu, S. B. Jo, A. K. Y. Jen, *Nano Energy* **2017**, *34*, 392.

[30] J. Pascual, G. Nasti, M. H. Aldamasy, J. A. Smith, M. Flatken, N. Phung, D. Di Girolamo, S. H. Turren-Cruz, M. Li, A. Dallmann, R. Avolio, A. Abate, *Mater. Adv.* **2020**, *1*, 1066.

[31] L. Wang, Z. Wang, H. Li, B. Chang, L. Pan, Z. Xie, L. Yin, *ACS Appl. Mater. Interfaces* **2022**, *14*, 18302.

[32] A. Halder, K. W. Yeom, N. G. Park, *ACS Energy Lett.* **2023**, *8*, 4267.

[33] T. Leijtens, R. Prasanna, A. Gold-Parker, M. F. Toney, M. D. McGehee, *ACS Energy Lett.* **2017**, *2*, 2159.

[34] M. I. Saidaminov, I. Spanopoulos, J. Abed, W. Ke, J. Wicks, M. G. Kanatzidis, E. H. Sargent, *ACS Energy Lett.* **2020**, *5*, 1153.

[35] B. Yang, D. Bogachuk, J. Suo, L. Wagner, H. Kim, J. Lim, A. Hinsch, G. Boschloo, M. K. Nazeeruddin, A. Hagfeldt, *Chem. Soc. Rev.* **2022**, *51*, 7509.

[36] M. Grischek, P. Caprioglio, J. Zhang, F. Peña-Camargo, K. Sveinbjörnsson, F. Zu, D. Menzel, J. H. Warby, J. Li, N. Koch,

E. Unger, L. Korte, D. Neher, M. Stolterfoht, S. Albrecht, *Sol. RRL* **2022**, *6*, 2200690.

[37] M. Stolterfoht, M. Grischek, P. Caprioglio, C. M. Wolff, E. Gutierrez-Partida, F. Peña-Camargo, D. Rothhardt, S. Zhang, M. Raoufi, J. Wolansky, M. Abdi-Jalebi, S. D. Stranks, S. Albrecht, T. Kirchartz, D. Neher, *Adv. Mater.* **2020**, *32*, 2000080.

[38] W. Tress, M. Yavari, K. Domanski, P. Yadav, B. Niesen, J. P. Correa Baena, A. Hagfeldt, M. Graetzel, *Energy Environ. Sci.* **2018**, *11*, 151.

[39] T. J. Savenije, D. Guo, V. M. Caselli, E. M. Hutter, *Adv. Energy Mater.* **2020**, *10*, 1903788.

[40] M. T. Klug, R. L. Milot, R. L. Milot, J. B. Patel, T. Green, H. C. Sansom, M. D. Farrar, A. J. Ramadan, S. Martani, Z. Wang, B. Wenger, J. M. Ball, L. Langshaw, A. Petrozza, M. B. Johnston, L. M. Herz, H. J. Snaith, *Energy Environ. Sci.* **2020**, *13*, 1776.

[41] D. Guo, V. M. Caselli, E. M. Hutter, T. J. Savenije, *ACS Energy Lett.* **2019**, *4*, 855.

[42] S. Siebentritt, T. P. Weiss, M. Sood, M. H. Wolter, A. Lomuscio, O. Ramirez, *J. Phys. Mater.* **2021**, *4*, 042010.

[43] D. Luo, R. Su, W. Zhang, Q. Gong, R. Zhu, *Nat. Rev. Mater.* **2020**, *5*, 44.